LAWRENCE
LIVERMORE
NATIONAL
LABORATORY

LLNL-PROC-655392

# Time-Resolved Measurements of the Hot-Electron Population in Ignition-Scale Experiments on the National Ignition Facility

M. Hohenberger, F. Albert, N. E. Palmer, J. J. Lee, T. Doeppner, L. Divol, E. L. Dewald, B. Bachmann, A. G. MacPhee, G. LaCaille, D. K. Bradley, C. Stoeckl

June 3, 2014

20th Topical Conference on High-Temperature Plasma Diagnostics
Denver, CO, United States
June 1, 2014 through June 5, 2014

## Disclaimer

# Time-Resolved Measurements of the Hot-Electron Population in Ignition-Scale Experiments on the National Ignition Facility[a)]

M. Hohenberger,[1, b)] F. Albert,[2] N. E. Palmer,[2] J. J. Lee,[3] T. Döppner,[2] L. Divol,[2] E. L. Dewald,[2] B. Bachmann,[2] A. G. MacPhee,[2] G. LaCaille,[2] D. K. Bradley,[2] and C. Stoeckl[1]

[1)] *Laboratory for Laser Energetics, University of Rochester, Rochester, New York 14623, USA*

[2)] *Lawrence Livermore National Laboratory, Livermore, California 94550, USA*

[3)] *National Security Technologies LLC, Livermore, CA 94551, USA*

(Dated: 4 June 2014)

In laser-driven inertial confinement fusion, hot electrons can preheat the fuel and prevent fusion-pellet compression to ignition conditions. Measuring the hot-electron population is key to designing an optimized ignition platform. The hot electrons in these high-intensity, laser-driven experiments, created via laser-plasma interactions, can be inferred from the bremsstrahlung generated by hot electrons interacting with the target. At the National Ignition Facility (NIF) [G. H. Miller *et al.*, Opt. Eng. **43**, 2841 (2004)], the filter-fluorescer x-ray (FFLEX) diagnostic–a multichannel, hard x-ray spectrometer operating in the 20- to 500-keV range–has been upgraded to provide fully time-resolved, absolute measurements of the bremsstrahlung spectrum with ∼300-ps resolution. Initial time-resolved data exhibited significant background and low signal-to-noise ratio, leading to a redesign of the FFLEX housing and enhanced shielding around the detector. The FFLEX x-ray sensitivity was characterized with an absolutely calibrated, energy-dispersive high-purity germanium detector (HPGe) using the high-energy x-ray (HEX) source [J. J. Lee *et al.*, Proc. SPIE **8505**, 850508 (2012)] at NSTec Livermore Operations over a range of K-shell fluorescence energies up to 111 keV (U $K_\beta$). The detectors impulse response function was measured *in-situ* on NIF short-pulse (∼90 ps) experiments, and in off-line tests.

## I. INTRODUCTION

In inertial confinement fusion (ICF), a capsule containing cryogenic deuterium–tritium (DT) fusion fuel is rapidly compressed to high temperatures and areal densities sufficient for thermonuclear fusion.[1] The goal of ICF research is to achieve a sustained thermonuclear burn, for which the energy released via the fusion burn is larger than the incident driver energy; i.e., the target ignites and the fusion gain exceeds unity. Current experiments at the National Ignition Facility (NIF)[2] aim at developing a laser-driven ICF platform, in which the fusion pellet is compressed at low entropy; i.e., the DT fuel is near Fermi degenerate. This is achieved with shaped laser pulses, either via direct laser irradiation of the implosion target (direct drive),[3] or using the indirect-drive approach.[4] Here the laser irradiates the inner walls of a high-$Z$ (typically Au) cavity (hohlraum) that surrounds the target, thereby generating a thermal x-ray bath that drives the ablative capsule implosion. A key concern in designing an optimized ignition platform is to limit the number of energetic electrons that are generated through plasma instabilities from the laser interacting with the ablating hohlraum walls or the capsule ablator material. These hot electrons can penetrate the ignition target and prematurely heat the fuel, raising the fuel adiabat and resulting in lower compression and reduced target performance. The mechanism and magnitude of hot-electron production can change during the targets evolution, and the acceptable level of hot-electron preheat increases as the capsule is being compressed.[5,6] A precise understanding of the history of hot-electron generation in ignition experiments is, therefore, vital for assessing its impact on the targets performance.[7] Here, we report on the filter-fluorescer x-ray (FFLEX) diagnostic that is used to measure the hard x-ray history and to infer the time-resolved, hot-electron population in ignition-scale experiments on the NIF. FFLEX has been in operation on the NIF as a time-integrated diagnostic since 2004.[8] It has recently been upgraded to provide temporal resolution. This paper describes the upgraded diagnostic and its characterization.

## II. THE FFLEX DIAGNOSTIC

The hot-electron population in ignition-scale experiments is typically described with a two-temperature distribution,[9] comprising a $T_1$∼20-keV component attributed to stimulated Raman scattering (SRS),[10] and a high-temperature component of $T_2$∼100 keV, attributed to the two-plasmon–decay instability.[11] The energetic electrons interact with the capsule ablator or the hohlraum walls, and lose energy via collisions and in the form of hard x-ray bremsstrahlung emission. A simple equation relating the measurable hard x-ray spectral-intensity distribution to a Maxwellian hot-electron population can be derived by balancing bremsstrahlung emission with the stopping power for energetic electrons.[12–14] This gives the thick-target bremsstrahlung equation for

[a)] Invited paper published as part of the Proceedings of the 20th Topical Conference on High-Temperature Plasma Diagnostics, Atlanta, Georgia, June, 2014.

[b)] mhoh@lle.rochester.edu

a one-temperature distribution

$$I\left(\frac{keV}{keV\,sr}\right) = \frac{5\times10^{11}}{4\pi}\frac{Z^*}{79}E_{hot,J}\exp\left(1-\frac{h\nu}{kT_{hot}}\right). \quad (1)$$

Here, $Z^* = \langle Z^2\rangle/\langle Z\rangle$ is the average atomic number, and $E_{hot,J}$ is the energy content in joules in the hot-electron component at temperature $kT_{hot}$.

To quantify the time-resolved hot-electron population in laser-driven experiments on the NIF, the absolutely calibrated FFLEX diagnostic measures the bremsstrahlung spectrum's temporal history in the 20- to 500-keV range using ten individually filtered, time-resolved detectors. FFLEX is positioned on the equator of the NIF target chamber at port (90,110). A schematic of channels 2 and 9 is shown in Fig. 1, with the inset showing a photograph of the FFLEX diagnostic mounted in the NIF target bay. Each channel comprises a fast $BaF_2$ scintillator, a UV filter, and a photomultiplier tube (PMT). $BaF_2$ has a decay time of ~700 ps and exhibits efficient absorption for x-ray energies as high as 500 keV. The UV filters have an ~40-nm bandpass centered at 220 nm and a peak transmittance of 30% to 40%. These filters isolate the 220-nm fast-decay component of $BaF_2$ from the 310-nm slow-decay component and reduce the light yield from the scintillator. The PMTs are Hamamatsu R5320 with a bialkali photocathode and an ~700-ps rise time. A negative bias ranging from 700 V to 2500 V can be applied to the photocathode to change its gain. The gain scales approximately with the seventh power of the bias, giving a dynamic operating range over roughly four orders of magnitude. The anode of the PMT is run directly to the 50-Ω input of a 2.5-GHz Tektronix oscilloscope that records the signal in steps of 100 ps. Each oscilloscope has four channels with two channels at different voltage scales dedicated to each FFLEX detector, and two FFLEX detectors sharing one oscilloscope. Timing is provided by an optical fiducial synchronized to the NIF laser clock at ~50 ns before the laser arrival, and with a timing jitter of less than 20 ps. This is combined with the FFLEX signal via an optical-to-electrical converter and gives an absolute reference to time the recorded x-ray signal relative to the laser pulse and the absolute experimental time.

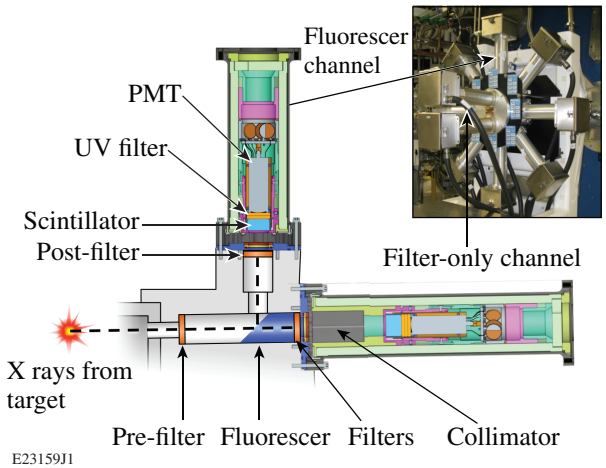


FIG. 1. Schematic of FFLEX Channels 2 and 9. Inset: photograph of the diagnostic mounted at the equator of the NIF target chamber.

TABLE I. Filter-fluorescer setup for channels 1–8

| Channel | Pre-filter, ($\mu$m) | Fluorescer, ($\mu$m) | Post-filter, ($\mu$m) |
|---|---|---|---|
| 1 | Mo, 91.0 | Y, 24.2 | Y, 18.9 |
| 2 | Sn, 74.3 | Y, 31.8 | Y, 22.5 |
| 3 | Sn, 353 | Ag, 34.1 | Ag, 6.8 |
| 4 | Mo, 113 | Ag, 29.6 | Ag, 9.5 |
| 5 | Ta, 526 | Yb, 170 | Yb, 42.2 |
| 6 | Pb, 794 | Yb, 160 | Yb, 40.4 |
| 7 | Pb, 801 | Au, 105 | Au, 25.5 |
| 8 | Ta, 525 | Au, 111 | Au, 25.8 |

Detectors 1–8 are arranged in a ring around the central axis of the diagnostic (see inset of Fig. 1) and use a combination of pre-filter, fluorescer, and post-filter to select an x-ray energy range. The fluorescer and pre-filter combination define the low-energy and high-energy cutoffs of the detector response with the channels designed in pairs of narrow- and broadband detectors that share the same low-energy cutoff. Detectors 9 and 10, extending out of the rear of the FFLEX diagnostic and away from the chamber center, employ filter-only setups that do not show the high-energy cutoff characteristic of the fluorescer channels. They are sensitive to hard x-ray emission above 100 keV and 200 keV, respectively. Channels 9 and 10 share the same line of sight as detec-

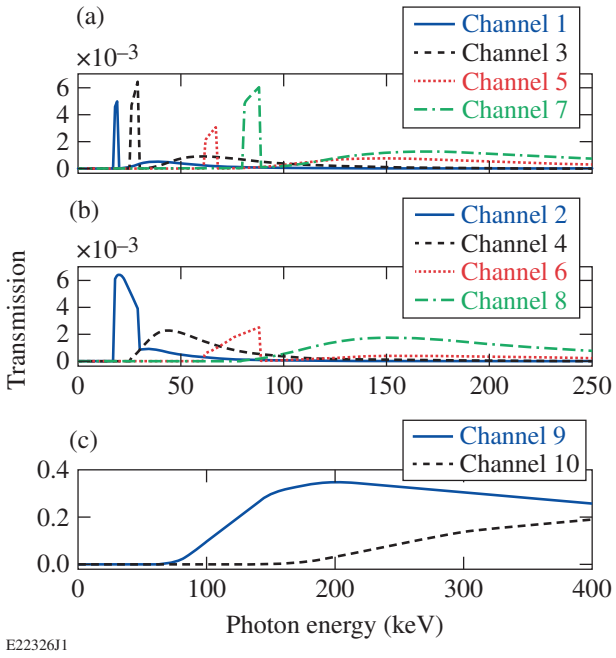


FIG. 2. FFLEX channel filter-transmission curves. Channels are paired in narrowband/broadband (odd/even channel number) combinations for Channels 1–8. Channels 9 and 10 are high-energy channels measuring $T_{hot}$ components above 100 keV.

TABLE II. Filter setup for channels 9 and 10

| Channel | Filter 1 | Filter 1 | Filter 3 | Filter 4 | Filter 5 |
|---|---|---|---|---|---|
| 9 | Sn, 74.3 $\mu$m | Y, 45.0 $\mu$m | Cu, 5mm | Al, 3 mm | – |
| 10 | Pb, 0.79 mm | Yb, 226 $\mu$m | Pt, 0.8 mm | Cu, 5mm | Al, 3 mm |

tors 2 and 6, respectively. Table I summarizes the filter and fluorescer setups of channels 1–8; the combination of filters used for the filter-only channels are listed in Table II. The transmission curves for the filter-fluorescer and filter-only setups are plotted in Fig. 2.

Sufficient shielding is necessary to ensure the detectors register only x-ray emission from the target interaction, and any recorded data is not compromised by scattered x-rays or electromagnetic interference (EMI). A major source of EMI is the laser–target interaction itself, but other diagnostics can also be significant sources of electromagnetic fields.[15] Each detector is separately assembled in a polyether ether ketone (PEEK) housing surrounded by an enclosure to shield the PMT's from EMI. Each assembly is located inside a Pb housing with a 1.25-cm wall thickness to shield the scintillator and PMT from x-ray emission not originating at the laser–target interaction. As part of the FFLEX upgrade from time-integrated to time-resolved detectors, the shielding was redesigned to fit the new detector size, but an initial version of the new FFLEX housing exhibited insufficient x-ray shielding around channels 1–8. This resulted in significant background, particularly at late times and after the end of the laser drive. The observed background was attributed to x rays scattering off neighboring diagnostics and the target bay walls. An example for a data set compromised by excessive background is displayed in Fig. 3(a), with the solid blue line showing raw FFLEX data and the dashed line marking the laser pulse.

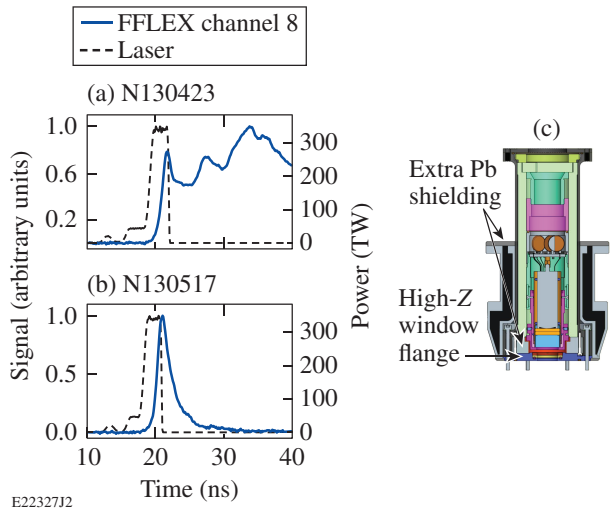


FIG. 3. FFLEX signal traces (a) before and (b) after upgrading the FFLEX shielding. The dashed line shows the laser-power profile and the solid line is the raw FFLEX waveform. As a result of the upgraded shielding shown in (c), the late-time background in the FFLEX data after the end of the laser pulse has been removed.

In this experiment (shot N130423) a NIF hohlraum was driven with ∼1.1-MJ and 350-TW peak power. The signal observed by FFLEX is expected to result from energetic electrons interacting with the Au plasma inside the hohlraum, and the hohlraum walls. Since the lifetime of these electrons is less than 100 ps, once the laser has turned off the FFLEX trace is expected to drop quickly on the time scale of the detector's decay time (∼3 ns, see Fig. 5). Instead, Fig. Fig. 3(a) shows significant signal after the end of the laser pulse, extending over tens of nanoseconds. These observations led to an upgrade of the shielding around channels 1–8, as shown in Fig. 3(c). The window flange was changed from Al to a tungsten alloy (Heavymet) and a Pb bracelet was added around each detector, increasing the lead shielding by 2.5 cm around the scintillator and PMT. Additionally, an EMI gasket was added to all ten channels in front of the window flange to enhance EMI protection [not shown in Fig.3(c)]. Figure3(b) shows raw FFLEX data of a recent shot (N130517) with very similar experimental conditions to the data from Fig. 3(a), but with the additional shielding deployed. As expected, the data in Fig. 3(b) does not exhibit the signal following the end of the laser pulse (dashed line). Note that the drawing and photograph in Fig. 1 show the original design without the additional shielding.

## III. CHARACTERIZATION

Calibrations were performed to quantify each detector's x ray sensitivity, PMT space-charge saturation, impulse response function (IRF), and the detector transit time. The absolute sensitivity of each FFLEX detector is determined by measuring the PMT's dc current while exposed to an x-ray source of known intensity and spectral composition. The high-energy x-ray source (HEX) at NSTec Livermore Operations served as a calibration source.[16] HEX uses a high-energy x-ray tube to excite K-shell fluorescence in a fluorescer foil and is capable of delivering near monoenergetic x-ray energies in the range of 8 keV (Cu $K_\alpha$) to 111 keV (U $K_\beta$). The x-ray emission is collimated and its total flux is measured with an absolutely calibrated, energy-dispersive high-purity germanium detector (HPGe). Placing an FFLEX channel in the same position as the HPGe reference exposes it to the same flux, thereby relating the FFLEX PMT current to the incident x-ray flux at a known K-shell energy. Taking the dark current into account for background subtraction, and multiplying with the 50-Ω input impedence of the oscilloscope, yields the channel sensitivity in units of Vns/keV. This relates the area under the oscilloscope waveform from an FFLEX detector to the x-ray energy incident on the scintillator for a given time interval.

To quantify the uncertainty of this measurement, the absolute sensitivity of a single FFLEX detector biased at –1700 V was measured in multiple configurations. This included measurements at different x-ray energies from 22 keV (Ag $K_\alpha$) to 111 keV (U $K_\beta$), with x-ray beams of different sizes and at two separate distances to the HEX source. Within the measurement error, the detector showed a flat response over the measured energy range, and the 14 individual setups yielded a standard deviation of 17% in the calculated sensitivity. The remaining FFLEX detectors were calibrated over the full operating bias range of –700 V to –2500 V in 200-V steps, with the x-ray source energies selected to match the operating range of the specific detector. Despite the calibration being limited to below ∼110 keV, the $BaF_2$ light yield per incident energy depends only weakly on the photon energy for photons above 100 keV, and the detector sensitivity is limited only by the x-ray stopping power of the scintillator.[17]

For signals of high enough magnitude, dynode-based PMT's saturate because of space-charge current limitations, as opposed to charge depletion. The PMT current reaches an upper limit and the output of the PMT temporally broadens. To avoid temporal broadening of the measured FFLEX signal, it is important to operate the detector below this space-charge saturation limit. The voltage on the oscilloscope at which signal broadening occurs was measured by focusing a 5-ns, 400-nm laser onto the photocathode of the PMT. By varying the incident energy, the signal was increased until the detector response started to broaden by >∼10%. To confirm that space-charge saturation had been reached, the laser intensity was then increased further by up to a factor 10. Figure 4(a) shows the average space-charge saturation limit as a function of the applied bias voltage, with the error bars denoting the highest and lowest values measured. To avoid nonlinearity effects prior to reaching the saturation limit, the detectors are typically operated at signal levels of ≤30% of the saturation limit.

The transit time of the electrons from the PMT photocathode to the anode is a function of the applied bias voltage. When correlating the measured x-ray trace to the absolute laser time, this variation must be taken into account. The transit time was measured by focusing an 80-ps, 400-nm laser pulse directly onto a PMT photocathode and comparing the laser arrival time, as measured by a photodiode, with the time of the measured PMT peak current. Figure 4(b) shows the difference in the delay between the peak signal on the photodiode and the PMT as a function of bias voltage. The transit time in nanoseconds is well fit by $t_{ns} = 10\sqrt{-2250/V_{bias,V}}$ where $V_{bias,V}$ is the applied photocathode bias voltage in volts.

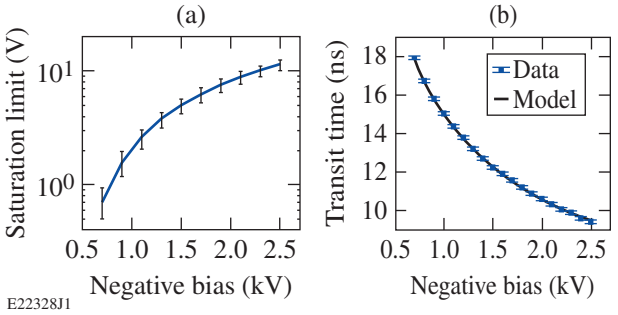


FIG. 4. (a) FFLEX space-charge limit of the signal voltage as a function of the applied bias. The solid line is the average of all ten detectors and the error bars denote minimum and maximum measured values. (b) PMT transit time as a function of the applied bias voltage.

A dedicated NIF timing shot was used to establish synchronization and absolute timing of all ten FFLEX channels. All 192 NIF beams delivered a laser pulse consisting of a 1-ns foot at ∼0.5 TW followed by an ∼90-ps, 80-TW laser impulse, with a total energy of ∼14 kJ. The laser was focused onto a 6-$\mu$m Au foil coated with 5 $\mu$m of CH. The laser prepulse ablates the CH coating, thereby setting up a plasma atmosphere that enhances coupling of the incident high-intensity impulse. This generates hot electrons that deposit their energy into the Au, giving hard x-ray emission concurrent with the laser impulse. The errors in determining the timing of peak emission, laser timing, and fiducial jitter, as well as that introduced by the PMT transit time, yield an uncertainty in the FFLEX oscilloscope traces of ∼170 ps. With a systematic uncertainty of the IRF of ∼150-ps (see below), the timing error after deconvolution increases to 230 ps.

Any x-ray signal recorded by FFLEX will be convolved with the system's IRF and to extract the temporal profile of the incident signal from the data, the detector's IRF must be accurately known. The x-ray IRF of two FFLEX detectors was measured off-line by the Comet laser at the Jupiter Laser Facility (JLF)[18] before installation on the NIF. A 5-J, 1053-nm, subpicosecond laser was focused onto a Cu target to generate an x-ray signal that was then recorded with individual FFLEX detectors. The experimental setup reproduced the NIF FFLEX setup; i.e., cabling, oscilloscope, etc. The FFLEX data is recorded on a 100-ps time base such that the x-ray emission from the Cu can be regarded as a $\delta$ function and the measured FFLEX signal is a direct representation of the system's response. Multiple measurements of the bias-dependent IRF's were obtained for a set of bias voltages on both detectors and, as expected, no significant variation of the system response was observed between the two FFLEX channels.

The NIF timing shot acted as an *in-situ* measurement of the detector's impulse response. Because of low signal, this is limited to high-gain settings with biases typically exceeding –2200 V. At these voltages, the *in-situ* rise and decay times of the detector's signals recorded on the NIF proved faster than the off-line measurements by ∼20%. This was confirmed in subsequent high-intensity laser-impulse experiments on the NIF. This indicates that the experimental setup for off-line measurements did not fully reproduce the setup used on the NIF. The off-line IRF's were scaled to match the *in-situ* response and the same 20% correction factor was applied to the IRF's used for lower bias settings. Figure 5 shows examples of the FFLEX IRF at various bias voltages. As expected, the impulse response becomes faster with increased bias since the PMT transit time is shortened and the current-waveform dispersion during transit from photocathode to

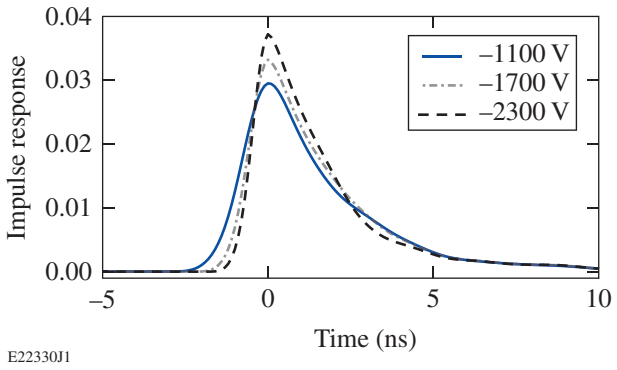


FIG. 5. FFLEX impulse response function at an operating bias of –1.1 kV (solid line), –1.7 kV (dashed–dotted line), and –2.3 kV (dashed line).

anode is reduced.

## IV. APPLICATIONS

The time-resolved FFLEX capabilities are an important addition to the NIF diagnostics suite. The time-resolved upgrade was fully implemented in May 2013 and in the following ten months, FFLEX was used for >70% of all NIF target shots. To infer the hot-electron population in NIF experiments, an exponentially falling hard x-ray spectrum with one or two temperature components following Eq. 1 is assumed. This is used to calculate the expected signal on the $i$th FFLEX channel for a given hot-electron population. By comparing the predicted signal to the experimental data, the hot-electron temperature and energy content are determined through an iterative fitting process and a $\chi^2$-minimization analysis. In hohlraum experiments, it was found that additionally including Au $K_\alpha$ and $K_\beta$ emission as a fitting parameter (rather than solving it self-consistently) significantly improves the quality of the fit.[9] An example for a time-integrated temperature analysis for a directly driven CH capsule (shot N131210) is shown Fig. 6. In this case the analysis converges to a single temperature distribution. The squares denote the measured x-ray emission for the ten FFLEX channels, and the solid line represents the fit through the data, giving a hot-electron component with a temperature of $T$=46±2 keV and an energy of $E$=2.5±0.2 kJ.

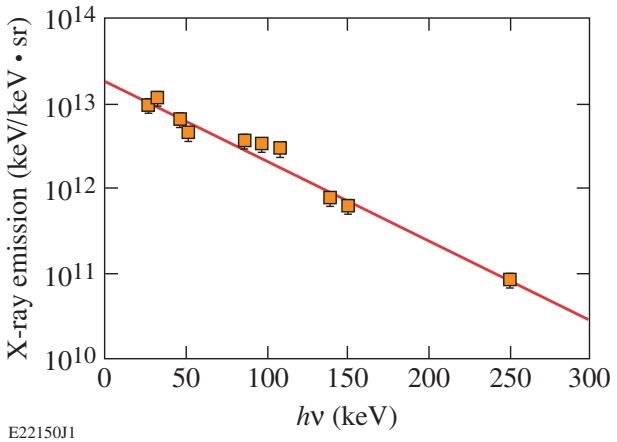


FIG. 6. Time-integrated FFLEX analysis for a directly driven CH shell (shot N131210). The squares are total emission as measured by the detector channels, the solid line is the inferred x-ray spectrum for a hot-electron component with 46±2-keV temperature and 2.5±0.2-kJ energy content.

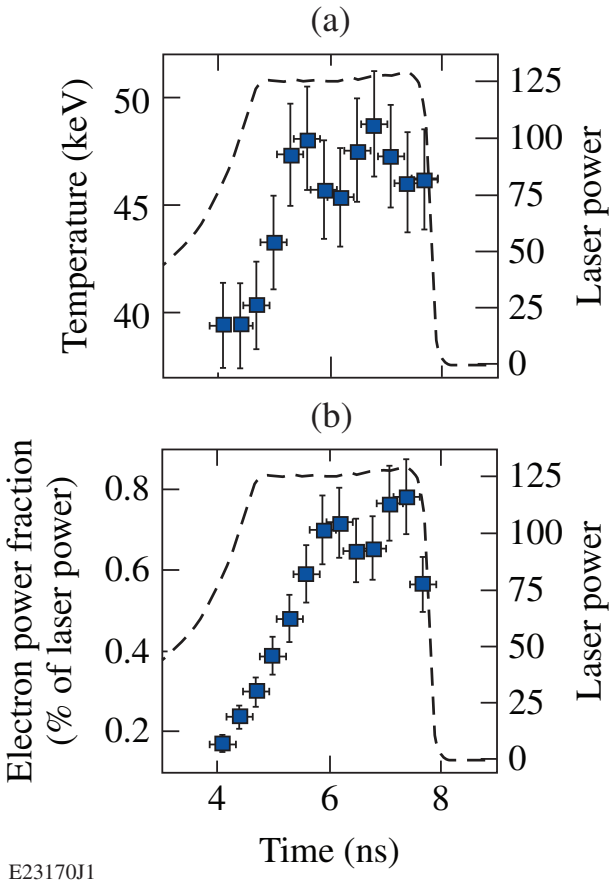


FIG. 7. Time-resolved FFLEX analysis for the data in Fig. 6, with (a) temperature and (b) emission power relative to the incident laser drive (dashed line).

To take advantage of the time-resolved capabilities of the upgraded FFLEX diagnostic, the oscilloscope waveforms are deconvolved to remove the detector-imposed IRF's and to produce a signal representative of the time-varying x-ray flux incident onto the FFLEX detector. The iterative deconvolution method of Nagy and Strakoš[19] is used, which is a modification of the steepest descent algorithm to minimize least-squares differences between the measured signal and the convolution of the deconvolved signal with the IRF. The time-resolved analysis for temperature and energy content of the data in Fig. 6 is shown in Figs. 7(a) and (b), respectively. In both plots the dashed line denotes the laser power incident onto the direct-drive target. The measured hard x-ray emission coincides with the high-intensity part of the drive laser. The emission rises quickly over ∼1.5 ns following the increased intensity of the laser drive, and then stays relatively stable at ∼47 keV with approximately 0.7% of the incident laser power being converted

into hot electrons. The signal rapidly drops into the noise once the laser has turned off.

## V. CONCLUSION

In conclusion, FFLEX is a hard x-ray detector at the National Ignition Facility that is used to infer the hot-electron population in high-energy density, ignition-scale experiments via hard x-ray emission measurement. The diagnostic consists of ten separate channels filtered to be sensitive to x rays in the 20- to 500-keV range. FFLEX has been in operation as a time-integrated diagnostic since 2004, but has recently been upgraded to provide absolutely calibrated, fully time-resolved measurements.

## ACKNOWLEDGMENTS

This material is based upon work supported by the Department of Energy National Nuclear Security Administration under Award Number DE-NA0001944, the University of Rochester, and the New York State Energy Research and Development Authority. Lawrence Livermore National Laboratory is operated by Lawrence Livermore National Security, LLC, for the U.S. Department of Energy, National Nuclear Security Administration under Contract DE-AC52-07NA27344. The support of DOE does not constitute an endorsement by DOE of the views expressed in this article. (LLNL-PROC-655392)

[1] S. Atzeni and J. Meyer-ter Vehn, *The Physics of Inertial Fusion: Beam Plasma Interaction, Hydrodynamics, Hot Dense Matter*, International Series of Monographs on Physics (Clarendon Press, Oxford, 2004).
[2] G. H. Miller, E. I. Moses, and C. R. Wuest, Opt. Eng. **43**, 2841 (2004).
[3] R. L. McCrory *et al.*, Phys. Plasmas **15**, 055503 (2008).
[4] J. D. Lindl, *Inertial Confinement Fusion: The Quest for Ignition and Energy Gain Using Indirect Drive* (Springer-Verlag, New York, 1998).
[5] E. L. Dewald *et al.*, J. Phys., Conf. Ser. **244**, 022074 (2010).
[6] E. L. Dewald *et al.*, Rev. Sci. Instrum. **81**, 10D938 (2010).
[7] C. Stoeckl, V. Y. Glebov, D. D. Meyerhofer, W. Seka, B. Yaakobi, R. P. J. Town, and J. D. Zuegel, Rev. Sci. Instrum. **72**, 1197 (2001).
[8] J. W. McDonald, R. L. Kauffman, J. R. Celeste, M. A. Rhodes, F. D. Lee, L. J. Suter, A. P. Lee, J. M. Foster, and G. Slark, Rev. Sci. Instrum. **75**, 3753 (2004).
[9] T. Döppner *et al.* Phys. Rev. Lett. **108**, 135006 (2012).
[10] A. A. Offenberger, R. Fedosejevs, W. Tighe, and W. Rozmus, Phys. Rev. Lett. 49, 371 (1982).
[11] S. P. Regan *et al.*, Phys. Plasmas **17**, 020703 (2010).
[12] K.A. Brueckner, Phys. Rev. Lett. **36**, 677 (1976).
[13] R. P. Drake *et al.*, Phys. Rev. A **40**, 3219 (1989).
[14] C. A. Thomas, Phys. Rev. E **81**, 036413 (2010).
[15] C. G. Brown Jr. *et al.*, Rev. Sci. Instrum. **83**, 10D729 (2012).
[16] J. J. Lee, M. J. Haugh, G. LaCaille, and P. Torres, Proc. SPIE **8505**, 850508 (2012).
[17] W. Mengesha, T. D. Taulbee, J. D. Valentine, and B. D. Rooney, Nucl. Instrum. Methods Phys. Res. A **486**, 448 (2002).
[18] S. R. Nagel *et al.*, Rev. Sci. Instrum. **83**, 10E116 (2012).
[19] J. Nagy and Z. Strakoš, Proc. SPIE **4121**, 182 (2000).